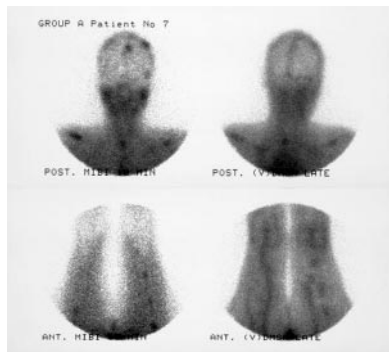


Wijns looks at the proliferation of non-invasive diagnostic tools in coronary artery disease and previews an article in this month's *JNM* on "noninvasive coronary angiography." **Page 904**

Gupta and colleagues outline the role of caspases in apoptosis and introduce important current research contributions on the potential for labeling caspase substrates in molecular imaging of apoptosis. **Page 906**



Isobe and colleagues investigate the use of early and delayed ^{123}I -MIBG scintigraphy in noninvasively assessing abnormal left ventricular functional reserve in response to exercise in patients with non-obstructive hypertrophic cardiomyopathy. **Page 909**

Kobayashi and colleagues evaluate the ability of ^{18}F -FDG PET coregistered with enhanced CT images to identify aortitis and localize and follow treatment response in patients with Takayasu arteritis. **Page 917**

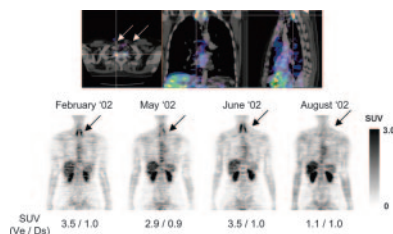
Knaapen and colleagues compare the perfusable tissue index, an alternative marker of myocardial fibrosis obtained using PET, with delayed contrast enhancement visualized by cardiac MRI in patients with hypertrophic cardiomyopathy. **Page 923**

Namdar and colleagues present a clinical evaluation of integrated PET/CT for combined acquisition of coronary anatomy and perfusion and note the promise of this technique for accurate, noninvasive clinical decision making about coronary artery disease. **Page 930**

Koeppel and colleagues compare the relative and complementary abilities of ^{11}C -dihydrotetrabenazine and ^{18}F -FDG PET measures in providing information useful in diagnosing dementias. **Page 936**

Chen and colleagues describe ^{18}F -FLT PET imaging of tumor cell proliferation in brain gliomas and report on side-by-side comparisons with ^{18}F -FDG PET studies in the same patients. . . **Page 945**

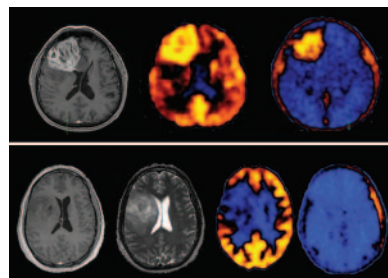
Yun and colleagues assess the role of gastric distension by ingestion of water as a cost-effective method for improving the diagnostic accuracy of ^{18}F -FDG PET in patients with suspected tumor recurrence in the remnant stomach. **Page 953**



Pakos and colleagues report on a meta-analysis of studies on ^{18}F -FDG PET in the evaluation of bone marrow infiltration in patients with lymphoma and compare these results with those from bone marrow biopsy. **Page 958**

Siessmeier and colleagues assess the comparative merits of voxelwise parametric mapping of ^{11}C -raclopride, ^{18}F -DMFP, and ^{18}F -fallypride in PET quantification of relative concentrations of dopamine $\text{D}_{2/3}$ receptors in the human brain. **Page 964**

Newberg and colleagues use ^{123}I -ADAM SPECT in patients with major depressive disorder to compare serotonin transporter binding with that in healthy individuals. **Page 973**



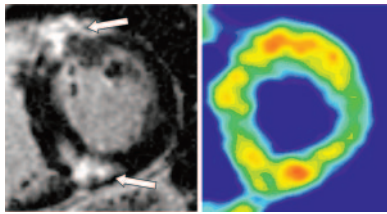
Koutsikos and colleagues investigate the combined use of $^{99\text{m}}\text{Tc}$ -sestamibi and $^{99\text{m}}\text{Tc}$ -V-DMSA scintigraphy in evaluating the effectiveness of chemotherapy in patients with multiple myeloma. . **Page 978**

Weber presents an educational review of the practical aspects of ^{18}F -FDG PET for treatment monitoring and techniques for performing quantitative assessment of tumor ^{18}F -FDG uptake in clinical studies. **Page 983**

Schäfers and colleagues evaluate the performance parameters of a commercial 32-module, high-performance small-animal PET scanner and report on their own experience in imaging with the system. **Page 996**

Constantinesco and colleagues report on the utility of in vivo pinhole gated SPECT in the establishment of a reference database for left ventricular myocardial perfusion, volumes, and motion in a normal mouse model. **Page 1005**

Bébé and colleagues describe the application of polyglutamic acids as a method for reducing anionic peptide uptake in the kidneys during radiopeptide therapy. **Page 1012**



van Schaijk and colleagues investigate the characteristics of a peptidase-resistant bivalent peptide to improve the residence time of ^{131}I in tumor pretargeting. . *Page 1016*

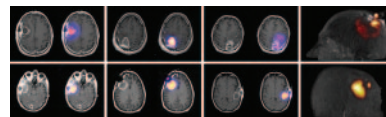
Stabin and colleagues document the basic functions of the OLINDA/EXM version 1.0 personal computer code and describe its similarities to and differences from the MIRDOSE radiation dosimetry software. *Page 1023*

la Fougère and colleagues assess striatal dopamine D_2 receptor availability by means of ^{123}I -IBZM SPECT in patients treated with high and low doses of amisulpride, a promising antipsychotic drug. . *Page 1028*

Shen and colleagues report on a method

for planning peripheral blood stem cell infusion time after high-dose radioimmunotherapy, based on noninvasive dosimetry that considers potential damage to the cells during circulation and residence times in organs with high radioactivity. *Page 1034*

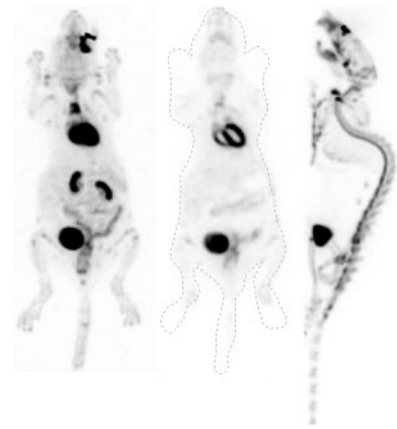
Akabani and colleagues evaluate dosimetry and dose-response relationships in patients with primary brain tumors treated with direct injections of ^{131}I -labeled anti-tenascin murine 81C6 monoclonal antibody into surgically created resection cavities followed by conventional external-beam therapy and chemotherapy. *Page 1042*



Zhang and colleagues describe an in vitro study in vascular smooth muscle cells to determine whether a $^{99\text{m}}\text{Tc}$ -labeled antisense oligonucleotide to the messenger RNA of proliferating cell nucleus antigen can be used for imaging of

atherosclerotic plaque and restenosis. *Page 1052*

Herzog and colleagues report on the effect of head motion on PET imaging of cerebral neuroreceptors and suggest ways in which the dynamic PET data may be corrected for head movement. . . . *Page 1059*



Bauer and colleagues look at the potential for using caspase substrates activated after the onset of apoptosis as an alternative target for apoptosis imaging and perform in vitro assessments of uptake and cell retention of these enzymes. *Page 1066*

ON THE COVER

On the left, a contrast-enhanced CT angiogram shows a stenotic lesion in the left circumflex coronary artery with faint poststenotic flow. In the center, a coronary angiogram shows the same stenotic lesion. On the right, a 3-dimensional reconstructed multislice spiral CT scan superimposed by a color-coded stress perfusion PET scan shows the coronary artery tree and the shape of the heart. Blue indicates a reversible perfusion defect. This image, by revealing a reduced hyperemic response to adenosine stress in the lateral wall, documents that the lesion seen in the first 2 images is hemodynamically relevant.

